

1 **A broadband active sound absorber with adjustable absorption coefficient and**
2 **bandwidth**

3

4 Kangkang Wang,¹ Li Shi,¹ Haishan Zou,^{1,a)} Sipei Zhao,² Chen Shen,³ and Jing Lu¹

5 ¹*Key Laboratory of Modern Acoustics, MOE, Institute of Acoustics, Department of Physics,*
6 *Nanjing University, Nanjing 210093, P. R. China*

7 ²*Centre for Audio, Acoustics and Vibration, Faculty of Engineering and IT, University of*
8 *Technology Sydney, Ultimo NSW 2007, Australia*

9 ³*Department of Mechanical Engineering, Rowan University, Glassboro, New Jersey 08028,*
10 *USA*

11

12 **Abstract:** Broadband adjustable sound absorbers are desired for controlling the acoustic
13 conditions within enclosed spaces. Existing studies on acoustic absorbers, either passive or
14 active, aim to maximize the sound absorption coefficients over an extended frequency band.
15 By contrast, this paper introduces a tunable acoustic absorber, whose working frequency band
16 and sound absorption characteristics can be defined by users for different applications. The
17 approach leverages an error signal that can be synthesized using a standing wave separation
18 technique. The error signal encodes different target reflection coefficients, leading to arbitrary
19 absorption coefficients between 0 and 1. Experimental validation is conducted in a one-
20 dimensional standing wave tube, demonstrating that the proposed active absorber achieves
21 near-perfect absorption within the 150–1600 Hz frequency range, boasting an average
22 absorption coefficient of 0.98. Adjustable absorption is demonstrated across three octave
23 bands, aligning closely with theoretical predictions. Furthermore, when coupled with a shaping
24 filter, the absorber exhibits spectrally tunable broadband absorption capabilities, selectively

^{a)}Email: hszou@nju.edu.cn

25 reflecting specific frequency bands while effectively absorbing others. These outcomes
26 underscore the versatile tunability of the proposed active acoustic absorber, which is expected
27 to pave the way for personalized regulating of the indoor acoustic environment.

28

29 **Keywords:** Broadband sound absorption, active control, standing wave separation, FeLMS
30 algorithm, flexible tunability

31

32 I. INTRODUCTION

33 As urbanization progresses, multipurpose rooms integrating audio rooms, concert halls,
34 and theatres are increasingly favored for their cost-effectiveness.¹ *Different functions in a*
35 *multipurpose room require different acoustic characteristics, including specific reverberation*
36 *and diffusion conditions*, with audio rooms requiring a low reverberation time to increase
37 speech intelligibility, while concert halls and theatres require a certain amount of reverberation
38 for optimal auditory experience. Traditionally, room reverberation has been manipulated
39 through methods like rotatable walls or rollable curtains to alter the absorption area of the room
40 walls.² However, these approaches are often unwieldy and demand considerable space,
41 particularly for managing low-frequency sound waves. Therefore, the development of flexibly
42 adjustable broadband absorbers is imperative to regulate room acoustics and achieve cost-
43 effective multifunctional spaces.

44 In recent years, the emergence of metamaterials has expanded the design possibilities for
45 tunable absorbers. Various subwavelength absorbers based on Helmholtz resonators,³⁻¹²
46 spatially folded Fabry-Pérot (FP) resonators¹³⁻²⁰ and thin film structures²¹⁻²⁶ have been
47 proposed. These absorbers offer adjustable acoustic absorption characteristics achieved by
48 modifying parameters such as the neck opening size⁵⁻¹⁰ and cavity volume^{11,12} of the Helmholtz
49 resonators, the effective length of the FP resonators,¹⁵⁻¹⁹ and the additional mass block of the

50 thin-film structures.^{21,22} These absorbers have shown promise in controlling sound fields in
51 room acoustics. For example, Qu *et al.*²⁷ designed a metamaterial absorber using a hybrid
52 structure comprising Helmholtz resonators and FP resonators to manipulate the reverberation
53 characteristics of a small room. This absorber can be precisely adjusted to achieve a
54 reverberation time of 0.1 s. A meta-equalizer is also proposed based on a combined resonator
55 structure. By manually switching on/off the resonators, functional filters, signal reproductions,
56 and sound-effect controls can be implemented.²⁸ Additionally, utilizing the thermoacoustic
57 effect is also a potential technical solution to design tunable sound absorbers.^{29,30} However,
58 their passive nature inherently restricts their tunability. Adjusting their acoustic performance
59 often necessitates mechanically altering their physical structures, posing practical challenges
60 in real-world applications.

61 To enhance the flexibility of regulating resonator characteristics, active control methods
62 can be introduced. Helmholtz resonators based on program-controlled motors have been
63 proposed,³¹ whose resonance frequency can be flexibly adjusted. A metasurface designed using
64 200 such tunable resonators can efficiently modulate the reverberant sound field in a room for
65 crosstalk-free acoustic communication. An active resonator can also be designed based on
66 impedance synthesis,³² which enables effective control of the resonant frequency and
67 bandwidth. Additionally, some scholars suggested that the voltage²⁴ or magnetic field²⁶ can be
68 applied to control the internal tension of the thin-film structures to modulate the sound
69 absorption performance of thin-film absorbers. Although these structures provide certain
70 adjustability, their strong resonance characteristics make them effective only in a narrow
71 bandwidth around the resonance frequency, which limits their broader applicability.

72 Recently, the shunt loudspeaker has garnered significant attention as a promising option
73 for designing tunable absorbers with broader bandwidth. This approach is based on the idea of
74 impedance synthesis, which can adjust the acoustic impedance of the loudspeaker diaphragm

75 by modulating the electrical impedance of the shunt circuit. Cong *et al.*³³ devised a multi-
76 resonance shunt circuit to expand the absorption bandwidth of the shunt loudspeaker.
77 Subsequently, they assessed the sound absorption capabilities of an array comprising 64 dual-
78 resonance shunted loudspeakers in a diffuse sound field within a reverberant room, achieving
79 near-perfect absorption at 100 Hz and 200 Hz.³⁴ Zhang *et al.*^{35,36} introduced the concept of a
80 shunted electro-magnetic diaphragm (SEMD), which is characterised by an RLC shunt circuit
81 based on a negative impedance converter to counteract the mechanical impedance of the
82 loudspeaker, thereby enabling broadband sound absorption. Ref. 36 presented an extensive
83 parametric analysis of shunted loudspeakers and proposed a methodology for designing
84 broadband tunable sound absorbers. Additionally, the shunt loudspeaker can also be combined
85 with other acoustic materials to enhance its performance, such as broadening the absorption
86 band when combined with a microperforated plate.^{35,37–39} Nevertheless, as a semi-active
87 absorber, the tunability of the shunt loudspeaker remains constrained, necessitating alterations
88 to the resistance, inductance, or capacitance in the shunt circuit to modulate its sound
89 absorption performance.

90 Active impedance synthesis with sensors can further enhance the sound absorption capacity
91 and modulation potential of a shunt loudspeaker, which can be programmed with a digital
92 controller to achieve a targeted impedance without changing any components within the circuit.
93 Boulandet *et al.*⁴⁰ conducted a comparative study on the efficacy of proportional feedback
94 control, proportional-integral-derivative (PID) control, and phase-compensated control
95 methods. Their findings indicate that PID and phase-compensated control techniques yield
96 superior results by mitigating the adverse effects of higher-order vibration modes in the
97 loudspeaker diaphragm. Rivet *et al.*⁴¹ proposed the control of current rather than voltage to
98 drive the loudspeaker, aiming to circumvent the deterioration of high-frequency acoustic
99 absorption by voice coil inductance and broaden the absorption bandwidth effectively.

100 Furthermore, a novel device called plasmacoustic metalayers is proposed to achieve impedance
101 synthesis through feedback control, enabling near-perfect acoustic absorption in the 20–2000
102 Hz frequency band.⁴² However, precise identification of the loudspeaker’s Thiele-Small (TS)
103 parameters is crucial for this non-adaptive control approach, and inevitable identification
104 deviation will deteriorate the sound absorption effect. Although mixed feedforward-feedback
105 architecture can help alleviate this problem,⁴³ the modelling process for loudspeaker-based
106 active impedance synthesis techniques primarily accounts for the piston vibration mode,
107 neglecting higher-order vibration modes, thus inherently constraining their effective
108 bandwidth.

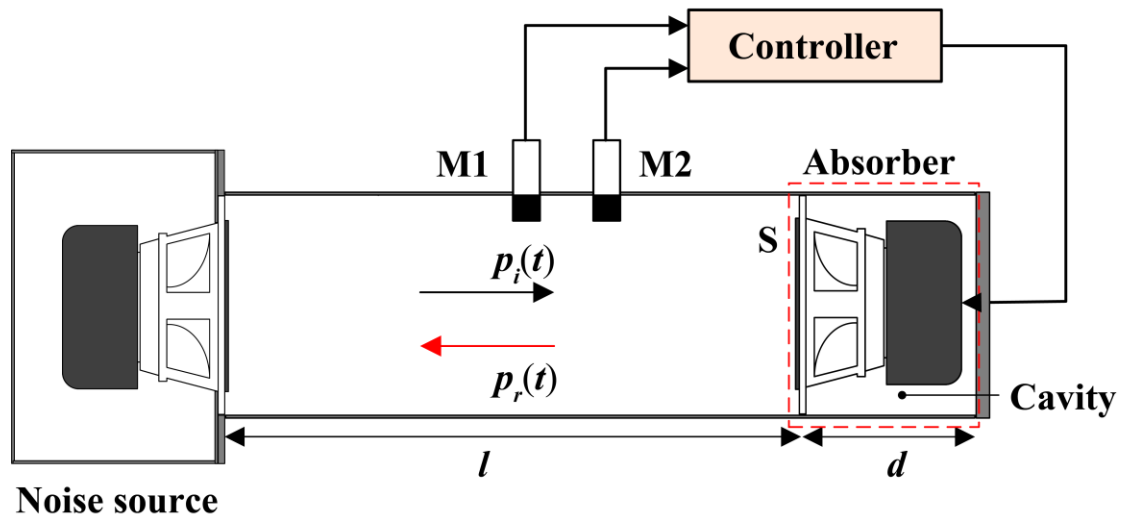
109 Adaptive active control techniques offer alternatives for absorber design, circumventing
110 the need for precise identification of loudspeakers’ TS parameters. Beyene *et al.*⁴⁴ proposed an
111 active-passive hybrid absorber employing an impedance matching strategy to actively cancel
112 the reflected waves separated by the two-microphone method, achieving efficient absorption
113 over a broad bandwidth (100–2000 Hz) with a coefficient exceeding 0.8. Additionally, Cobo
114 *et al.*⁴⁵ developed an analytical model to compare the efficacy of impedance matching and
115 pressure release strategies. It is revealed that the pressure release method outperforms
116 impedance matching when the flow resistance of porous materials matches air’s characteristic
117 acoustic impedance. Subsequently, a large-area active absorber panel was designed based on
118 the pressure release strategy, and it could achieve up to 0.94 absorption in the frequency range
119 of 266–1500 Hz even for obliquely incident waves at a 20° angle of incidence.⁴⁶ Because of
120 these hybrid active absorbers, combining active units with passive absorbing materials in a
121 cascade form, often results in considerable thickness. Employing adaptive impedance control
122 techniques, An *et al.*⁴⁷ proposed a hybrid absorber with a parallel form with a thickness of only
123 80 mm and an absorption performance exceeding 0.9 above 20 Hz. However, most of these

124 studies focus on enhancing sound absorption efficiency across a broader frequency range, and
125 the broadband tunability of active absorbers remains largely unexplored.

126 In this paper, we present a flexibly tunable active sound absorber, which can attain arbitrary
127 absorption coefficients ranging from 0 to 1 across more than three octave bands by regulating
128 the target reflection coefficient. Moreover, in combination with the filtered-e least mean square
129 (FeLMS) algorithm⁴⁸ and a band-stop filter, this active absorber can achieve spectrally tunable
130 broadband acoustic absorption. Experiments are conducted to exemplify the flexible tunability
131 of the designed active absorber, without necessitating any alterations to its physical structure.
132 This absorber is expected to provide a rich means of adjustment for the individualized acoustic
133 environment requirements of multipurpose rooms.

134 The remainder of this paper is organized as follows. Section 2 presents the control
135 mechanism and algorithm of our active absorber, which are compared with the existing design
136 scheme. In Section 3, experiments are carried out in a standing wave tube to validate the
137 effectiveness of the designed active absorber, and arbitrarily adjustable absorption coefficients
138 between 0 and 1 are realized. Subsequently, a spectrally tunable broadband absorption effect
139 is demonstrated with the use of a band-stop filter. Finally, conclusions are summarized in
140 Section 4.

141



142

143 FIG. 1. (Color online) The schematic diagram of the designed active absorber. The main
 144 structure of the absorber with thickness d is marked by the red dashed box, which contains the
 145 loudspeaker and the cavity.

146

147 II. THEORY

148 The configuration of the active sound absorber is shown in Fig. 1. The physical structure
 149 of the absorber is marked in the red dashed box, and consists of a loudspeaker in air and the
 150 cavity between the loudspeaker and the hard boundary backing. Two microphones $M1$ and $M2$
 151 are located in front of the absorber and are utilized to separate the incident and reflected waves
 152 in the one-dimensional standing wave tube to generate the error signal, which is the difference
 153 between the desired signal and the output signal of the active absorber. The energy of the error
 154 signal is minimized by manipulating the secondary source through a controller, facilitating
 155 broadband control with adjustable acoustic absorption performance.

156

157 **A. Current active absorber**

158 Let the incident wave sound pressure be $p_i(t)$ and the reflected wave sound pressure be $p_r(t)$
159 at microphone M1, then the total sound pressure $p_1(t)$ is:

160
$$p_1(t) = p_i(t) + p_r(t). \quad (1)$$

161 When the spacing between microphones M1 and M2 is s , the acoustic time delay between them
162 is $\tau = s/c_0$, where c_0 is the speed of sound in air. Moreover, given that the tube's radius is
163 significantly larger than the boundary layer thickness and this paper focuses on low and
164 medium frequency bands below 2000 Hz, the viscothermal loss of sound waves in this tube is
165 minimal and can be reasonably neglected. Therefore, the total sound pressure $p_2(t)$ at
166 microphone M2 can be expressed as

167
$$p_2(t) = p_i(t - \tau) + p_r(t + \tau). \quad (2)$$

168 The Fourier transform of Eqs. (1) and (2) yields

169
$$P_1(\omega) = P_i(\omega) + P_r(\omega), \quad (3)$$

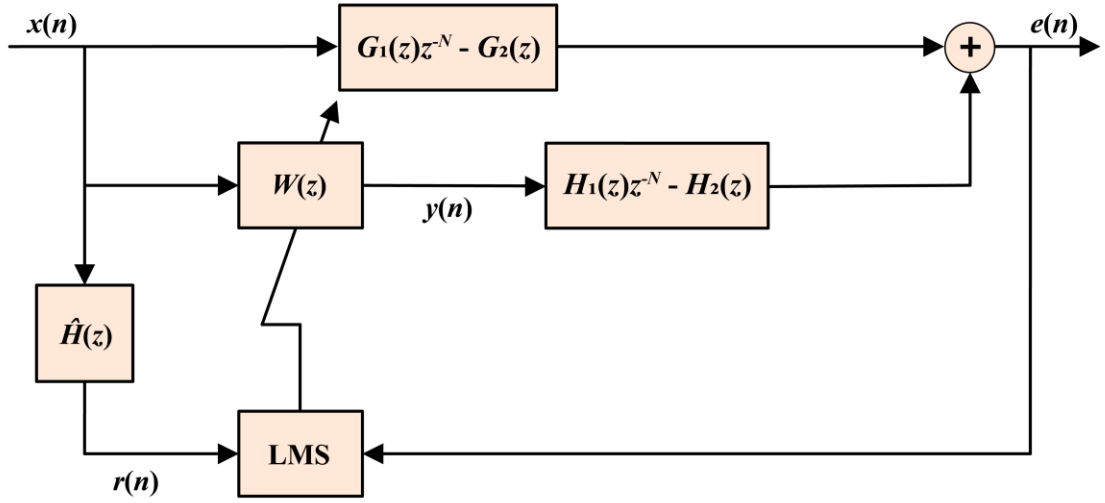
170
$$P_2(\omega) = P_i(\omega)e^{-j\omega\tau} + P_r(\omega)e^{j\omega\tau}. \quad (4)$$

171 The incident and reflected waves can be extracted from Eqs. (3) and (4) as follows

172
$$P_i(\omega)(e^{-2j\omega\tau} - 1) = P_2(\omega)e^{-j\omega\tau} - P_1(\omega), \quad (5)$$

173
$$P_r(\omega)e^{j\omega\tau}(e^{-2j\omega\tau} - 1) = P_1(\omega)e^{-j\omega\tau} - P_2(\omega). \quad (6)$$

174



175

176 FIG. 2. (Color online) Module diagram illustrating the FxLMS algorithm for current active
 177 absorbers.

178

179 The primary objective of current active absorber designs is to achieve efficient broadband
 180 sound absorption by cancelling reflected waves.^{44,49} Control algorithms for such systems often
 181 leverage the filtered-x least mean square (FxLMS) algorithm,⁵⁰ whose module diagram is
 182 depicted in Fig. 2. In this diagram, $W(z)$ represents the z -transform⁵¹ of the control filter $\mathbf{w}(n)$.
 183 $x(n)$ refers to the reference signal, $r(n)$ is the filtered-x signal, $y(n)$ is the control signal fed to
 184 the control source, and $e(n)$ denotes the error signal. $G_1(z)$ and $G_2(z)$ represent the primary paths
 185 from the noise source to microphones M1 and M2, while $H_1(z)$ and $H_2(z)$ denote the secondary
 186 paths from the secondary source to microphones M1 and M2, respectively. The sound
 187 absorption performance depends on the amplitude of the reflected wave $P_r(\omega)$ and is
 188 independent of its phase. Given the amplitude for the coefficient of $P_r(\omega)$ on the left side of the
 189 Eq. (6) is a constant, the error signal can be defined accordingly as

190
$$E(\omega) = P_1(\omega)e^{-j\omega\tau} - P_2(\omega). \quad (7)$$

191 The corresponding z -domain error signal $E(z)$ of Eq. (7) can be expressed as

192
$$E(z) = P_1(z)z^{-N} - P_2(z), \quad (8)$$

193 where $N = \tau f_s$ and f_s represents the sampling rate of the system. Meanwhile, $P_1(z)$ and $P_2(z)$ can
 194 also be represented by the primary sound pressure and the secondary sound pressure, i.e.,

195
$$P_1(z) = P_{1p}(z) + P_{1s}(z), \quad (9)$$

196
$$P_2(z) = P_{2p}(z) + P_{2s}(z), \quad (10)$$

197 where $P_{1p}(z) = X(z)G_1(z)$ and $P_{1s}(z) = Y(z)H_1(z)$ represent the primary and secondary acoustic
 198 signals at microphone M1 respectively, while $P_{2p}(z) = X(z)G_2(z)$ and $P_{2s}(z) = Y(z)H_2(z)$ denote
 199 the primary and secondary acoustic signals at microphone M2 respectively. $X(z)$ and $Y(z)$ are
 200 the z -transform of the reference signal $x(n)$ and the secondary source signal $y(n)$, respectively.

201 Bringing Eqs. (9) and (10) into Eq. (8) yields

202
$$E(z) = X(z)[G_1(z)z^{-N} - G_2(z)] + Y(z)[H_1(z)z^{-N} - H_2(z)]. \quad (11)$$

203 At this point, microphones M1 and M2 can be considered as a virtual microphone, termed M.
 204 The primary path of the virtual microphone M is $G(z) = G_1(z)z^{-N} - G_2(z)$, while the secondary
 205 path is $H(z) = H_1(z)z^{-N} - H_2(z)$, as shown in Fig. 2. The corresponding time-domain error signal
 206 $e(n)$ of Eq. (8) can be calculated by the inverse z -transform as

207
$$e(n) = p_1(n - N) - p_2(n). \quad (12)$$

208 To minimize the energy of the error signal $e(n)$, the cost function $J(n)$ is defined as

209
$$J(n) = E[e^2(n)], \quad (13)$$

210 where $E(\cdot)$ is the expectation operator. Following the FxLMS algorithm, the update formula for
 211 the control filter coefficients $\mathbf{w}(n)$ can be derived as⁵⁰

212
$$\mathbf{w}(n+1) = \mathbf{w}(n) - 2\mu e(n)\mathbf{r}(n), \quad (14)$$

213 where μ represents the convergence coefficient, $\mathbf{r}(n)$ is the filtered-x signal vector, which is
 214 obtained by filtering the reference signal $\mathbf{x}(n)$ by the secondary path model $\hat{\mathbf{h}}(n)$. $\hat{\mathbf{h}}(n) = \hat{\mathbf{h}}_1(n -$

215 $N) - \hat{\mathbf{h}}_2(n)$ is the the impulse response of the secondary path estimation $\hat{H}(z)$ in Fig. 2, with
 216 $\hat{\mathbf{h}}_1(n)$ and $\hat{\mathbf{h}}_2(n)$ being estimates of the true secondary paths $\mathbf{h}_1(n)$ and $\mathbf{h}_2(n)$ respectively.

217

218 **B. Proposed adjustable active absorber**

219 To expand the tunability of the absorber, this paper introduces a scheme that can not only
 220 realize broadband absorption with arbitrarily adjustable absorption coefficients, but also
 221 tunable absorption spectra where reflection is still enabled within certain frequency bands.
 222 Since the reflection coefficient is expressed as $R = P_r/P_i$, combining Eqs. (5) and (6) yields

$$223 \quad R(\omega) = e^{-j\omega\tau} \cdot \frac{P_1(\omega)e^{-j\omega\tau} - P_2(\omega)}{P_2(\omega)e^{-j\omega\tau} - P_1(\omega)}. \quad (15)$$

224 Likewise, only controlling the amplitude of the reflection coefficient is enough to achieve a
 225 specific sound absorption coefficient. According to Eq. (15), the error signal $E(\omega)$ can be
 226 defined as

$$227 \quad E(\omega) = P_1(\omega)e^{-j\omega\tau} - P_2(\omega) - R_0(P_2(\omega)e^{-j\omega\tau} - P_1(\omega)), \quad (16)$$

228 where R_0 is the target reflection coefficient, which corresponds to the desired target absorption
 229 coefficient $A_0 = 1 - |R_0|^2$. The corresponding z -domain error signal $E(z)$ of Eq. (16) can also be
 230 formulated as

$$231 \quad E(z) = P_1(z)z^{-N} - P_2(z) - R_0(P_2(z)z^{-N} - P_1(z)). \quad (17)$$

232 Bringing Eqs. (9) and (10) into Eq. (17) yields

$$233 \quad E(z) = X(z)[G_1(z)z^{-N} - G_2(z) - R_0(G_2(z)z^{-N} - G_1(z))] \\ + Y(z)[H_1(z)z^{-N} - H_2(z) - R_0(H_2(z)z^{-N} - H_1(z))]. \quad (18)$$

234 Therefore, the primary path of the virtual microphone M is converted as $G(z) = G_1(z)z^{-N} - G_2(z)$
 235 $- R_0(G_2(z)z^{-N} - G_1(z))$, while the secondary path is converted as $H(z) = H_1(z)z^{-N} - H_2(z) -$
 236 $R_0(H_2(z)z^{-N} - H_1(z))$. The corresponding time-domain error signal $e(n)$ of Eq. (17) can also be
 237 calculated by the inverse z -transform as

238
$$e(n) = p_1(n - N) - p_2(n) - R_0(p_2(n - N) - p_1(n)). \quad (19)$$

239 The target absorption coefficient A_0 is obtained by minimizing the energy of $e(n)$ in Eq. (19).
 240 In contrast to Eq. (12), which requires only the reflected wave to achieve perfect broadband
 241 absorption, the proposed approach leverages both incident and reflected wave information to
 242 attain broadband absorption with adjustable absorption coefficients.

243 The control algorithm can be implemented using the FeLMS algorithm,⁴⁸ illustrated in Fig.
 244 3. Compared to Fig. 2, the primary and secondary path models contain information about
 245 incident and reflected sound, allowing the algorithm to achieve broadband sound absorption
 246 with adjustable coefficients by setting different target reflection coefficients R_0 . Additionally,
 247 a shaping filter $\mathbf{f}(n)$ is applied based on the FeLMS algorithm to filter the error signal and
 248 reference signal before updating the control filter $\mathbf{w}(n)$. This constrains the frequency band of
 249 the control filter and achieves spectrally tunable broadband sound absorption. In Fig. 3, $F(z)$
 250 within the light blue box signifies the z -transform of the shaping filter $\mathbf{f}(n)$. The filtered error
 251 signal $e'(n)$ is obtained by filtering the error signal $e(n)$ by the shaping filter $F(z)$, i.e., $e'(n) =$
 252 $e(n) * f(n)$, and the cost function is correspondingly modified to $J'(n)$ as

253
$$J'(n) = E[e'^2(n)]. \quad (20)$$

254 Like the derivation of the FxLMS algorithm, the update formula for the controller $\mathbf{w}(n)$ in the
 255 FeLMS algorithm can be derived as

256
$$\mathbf{w}(n+1) = \mathbf{w}(n) - 2\mu e'(n)\mathbf{r}'(n), \quad (21)$$

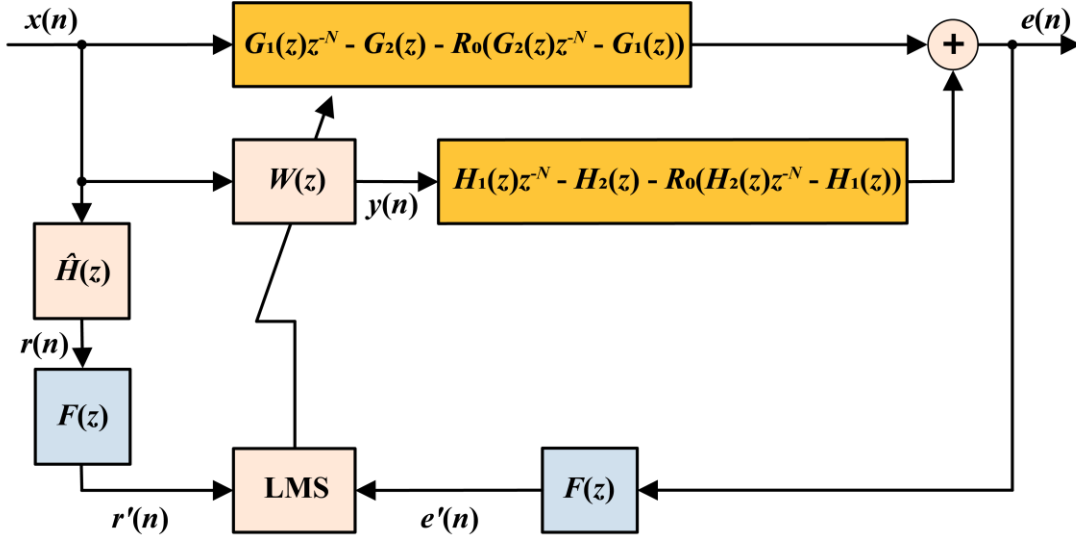
257 where $\mathbf{r}'(n)$ is the signal vector obtained by filtering $\mathbf{r}(n)$ by the shaping filter $F(z)$, i.e., $r'(n) =$
 258 $r(n) * f(n)$. At this point, the secondary path estimate $\hat{\mathbf{h}}(n)$ that generates the filtered reference
 259 signal vector $\mathbf{r}(n)$ is expressed as $\hat{\mathbf{h}}(n) = \hat{\mathbf{h}}_1(n - N) - \hat{\mathbf{h}}_2(n) - R_0(\hat{\mathbf{h}}_2(n - N) - \hat{\mathbf{h}}_1(n))$.

260 In the case where $F(z) = 1$, the FeLMS algorithm reverts to the FxLMS algorithm. In this
 261 scenario, the active absorber modulates solely the absorption coefficients according to the
 262 specified target reflection coefficient R_0 . The update formula for the control filter $\mathbf{w}(n)$ in Eq.

263 (21) is formally simplified as in Eq. (14), however, $e(n)$ and $\mathbf{r}(n)$ are different between the two.

264 The two formulas are identical only when $R_0 = 0$.

265



266

267 FIG. 3. (Color online) Module diagram illustrating the control algorithm for the designed active

268 absorber.

269

270 **III. EXPERIMENTS**

271 To validate the effectiveness of the proposed active absorber, experiments were conducted

272 in a circular standing-wave tube shown in Fig. 4 with a diameter of $d_0 = 12$ cm, which has a

273 cutoff frequency of 1658 Hz for the plane wave mode. The tube wall is made of 20 mm thick

274 plexiglass, which provides good sound insulation, predicted by the mass law to exceed 25 dB

275 above 150 Hz. The primary noise source, powered by an amplifier, was positioned at the left

276 end of the tube, while the active absorber was placed at the opposite end, maintaining a spacing

277 of $l = 1.5$ m. Acoustic foams were placed in front of the noise source to mitigate the influence

278 of multiple sound wave reflections within the tube. The active absorber consists of a 4-inch

279 Hivi B4N loudspeaker (see detailed Thiele&Small parameters in Supplementary Table SI) and

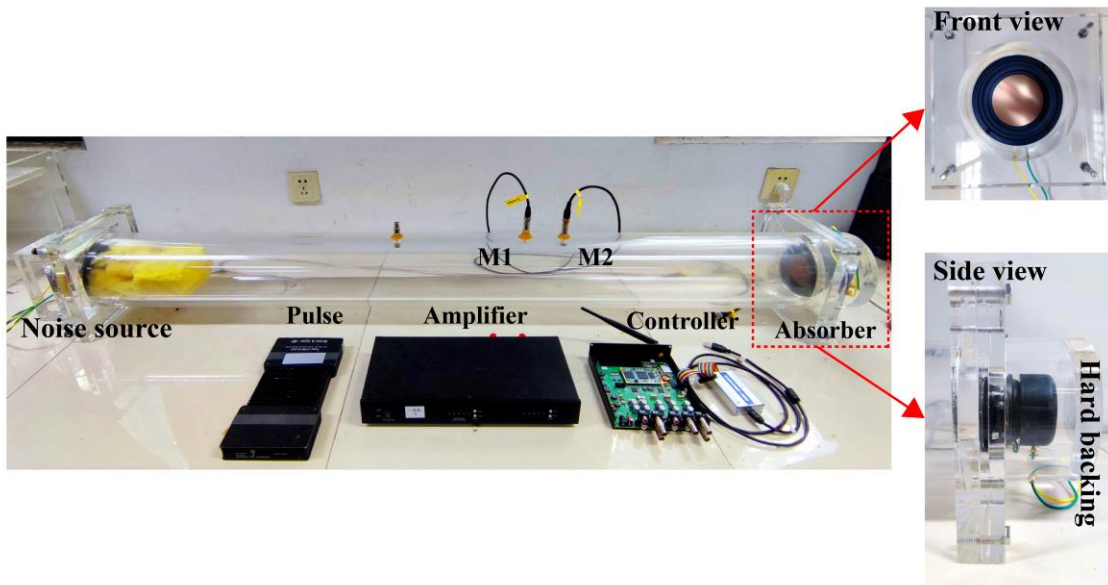
280 a cavity behind it with a thickness of $d = 82.5$ mm, surrounded by a 20 mm thick plexiglass
 281 plate that can be considered as a hard boundary. To simplify the design of the experimental
 282 system, microphones M1 and M2 with a spacing of $s = 8$ cm were employed as error
 283 microphones for the active absorber as well as measurement microphones. The absorption
 284 coefficients of active absorbers could be measured based on the transfer function method. The
 285 resulting measured sound absorption coefficient is denoted as A_{mea} , i.e.,

$$286 \quad A_{\text{mea}} = 1 - |R_{\text{mea}}|^2, \quad (22)$$

$$287 \quad R_{\text{mea}} = \frac{H_{12} - H_1}{H_R - H_{12}} e^{j2kx_1}, \quad (23)$$

288 where $H_{12} = p_2/p_1$ is the transfer function between the sound pressure signals measured by
 289 microphones M2 and M1, and $H_1 = e^{-jks}$, $H_R = e^{jks}$. $k = \omega/c_0$ denotes the wave number in air,
 290 and x_1 refers to the distance from microphone M1 to the interface **S** of the active absorber.

291



292
 293 FIG. 4. (Color online) Photograph of the experimental setup based on a one-dimensional
 294 standing wave tube. The two subfigures depict the front and side views of the active absorber.

295

296 During the experiments, to exclusively excite the plane wave mode, a low-pass white noise
297 signal below 1600 Hz is generated by the B&K Pulse, which is then amplified to drive the
298 noise source. Simultaneously, the signal is also fed into the controller to serve as the reference
299 signal. The controller is implemented by employing a TMS320C6748 chip with a sampling
300 rate of $f_s = 16000$ Hz and a 1024-tapped FIR filter is embedded. The identification of secondary
301 paths $\mathbf{h}_1(n)$ and $\mathbf{h}_2(n)$ is conducted using the least mean square (LMS) algorithm, employing
302 two 512-tapped FIR filters with an modelling accuracy of up to 25 dB.

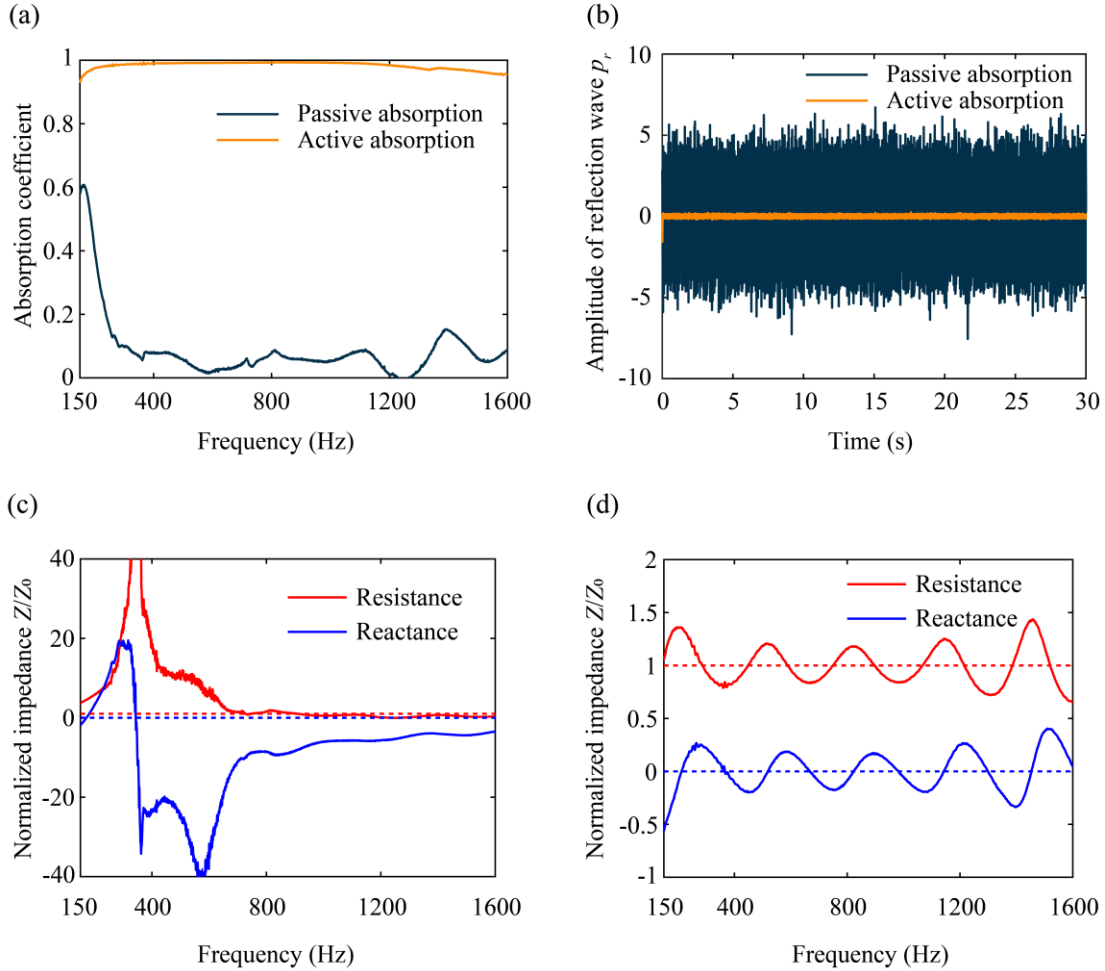
303

304 **A. Realization of arbitrarily adjustable sound absorption coefficients**

305 The shaping filter $F(z) = 1$ in Fig. 3 is set to explore the broadband sound absorption
306 performance and adjustability of the absorption coefficient of the designed active absorber.
307 Initially, the active sound absorption effect under the perfect absorption ($R_0 = 0$) condition is
308 compared with the passive sound absorption effect, with results depicted in Fig. 5(a). Passive
309 absorption denotes performance achieved by deactivating the active control and relying solely
310 on the sound absorption capacity of the secondary source loudspeaker. It can be seen that in
311 the 150–1600 Hz frequency band, the average sound absorption coefficient is merely 0.09,
312 indicating poor performance in this scenario. By turning on the active control function and
313 setting $R_0 = 0$ in the error signal, the active absorber can realize near-perfect broadband
314 absorption performance in the frequency band of 150–1600 Hz with an average absorption
315 coefficient of 0.98 when the controller converges. Fig. 5(b) compares the reflected wave
316 amplitudes for passive and active absorption to further demonstrate the attenuation of reflected
317 wave energy by the active absorber. The results demonstrate that the designed active absorber
318 significantly reduces the reflected wave energy and achieves near-perfect sound absorption.
319 This is attributed to the controller adjusting the acoustic impedance at the secondary source

320 interface \mathbf{S} to match the characteristic acoustic impedance Z_0 of the air (refer to Fig. 5(c), (d)),
 321 thereby significantly enhancing the absorption performance of the absorber.

322



323

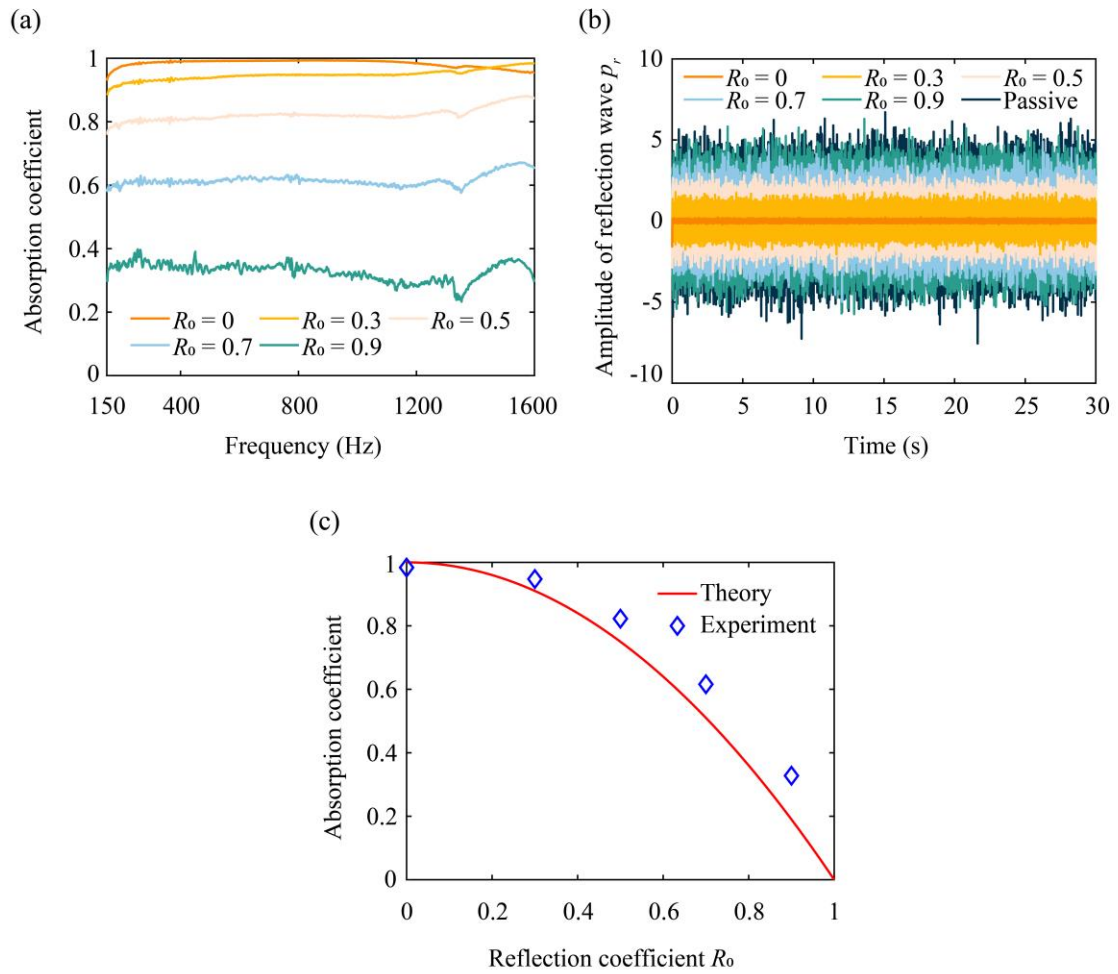
324 FIG. 5. (Color online) Comparison of the active absorption performance under the perfect
 325 absorption condition ($R_0 = 0$) with passive absorption solely by the secondary source
 326 loudspeaker. (a) Spectra of absorption coefficients for passive and active absorption. (b) The
 327 remaining amplitude of reflected waves after passive and active absorption. (c–d) Normalized
 328 acoustic impedance at the absorber interface \mathbf{S} for passive and active absorption. This acoustic
 329 impedance can be derived from the measured reflection coefficient R_{mea} , i.e., $Z/Z_0 = (1 +$
 330 $R_{\text{mea}})/(1 - R_{\text{mea}})$, where $Z_0 = \rho_0 c_0$ is the characteristic acoustic impedance of air. The red dashed

331 line indicates the real part of Z_0 , while the blue dashed line indicates the imaginary part of Z_0 ,
332 providing a reference for evaluating the matching degree between the acoustic impedance at
333 the absorber interface \mathbf{S} and that of air.

334

335 The designed active absorber also enables broadband absorption with arbitrarily adjustable
336 absorption coefficient by setting different target reflection coefficients R_0 in the error signal
337 when the shaping filter $F(z) = 1$. Five cases of $R_0 = 0, 0.3, 0.5, 0.7, 0.9$ are demonstrated and
338 the results are shown in Fig. 6(a). When the controller converges, the active absorber exhibits
339 flat broadband absorption spectra with adjustable absorption coefficients within the 150–1600
340 Hz frequency band, showing an effective control bandwidth exceeding 3 octaves. The residual
341 amplitude of the reflected wave is compared across different R_0 values in Fig. 6(b), as expected
342 decreasing R_0 results in a reduction of the residual reflected wave amplitude. The average
343 absorption coefficients of the measured absorption spectra within the 150–1600 Hz band for
344 these five cases are 0.98, 0.94, 0.82, 0.62, and 0.33, respectively, aligning well with the
345 theoretical absorption coefficient $A_0 = 1 - |R_0|^2$, as shown in Fig. 6(c). The slight deviation can
346 be attributed to the fact that the acoustic time delay τ between microphones M1 and M2 results
347 in a non-integer sampling point $N = \tau f_s$, which had to be rounded off due to the utilization of a
348 digital signal processor (DSP) in the experiments. Although only five cases are illustrated here,
349 it is reasonable to infer that the designed active absorber can achieve arbitrary absorption
350 coefficients ranging from 0 to 1, showcasing its versatile broadband tunability. This capability
351 holds significant potential for optimizing acoustic characteristics in multipurpose rooms where
352 different absorption coefficients and reverberation times are needed.

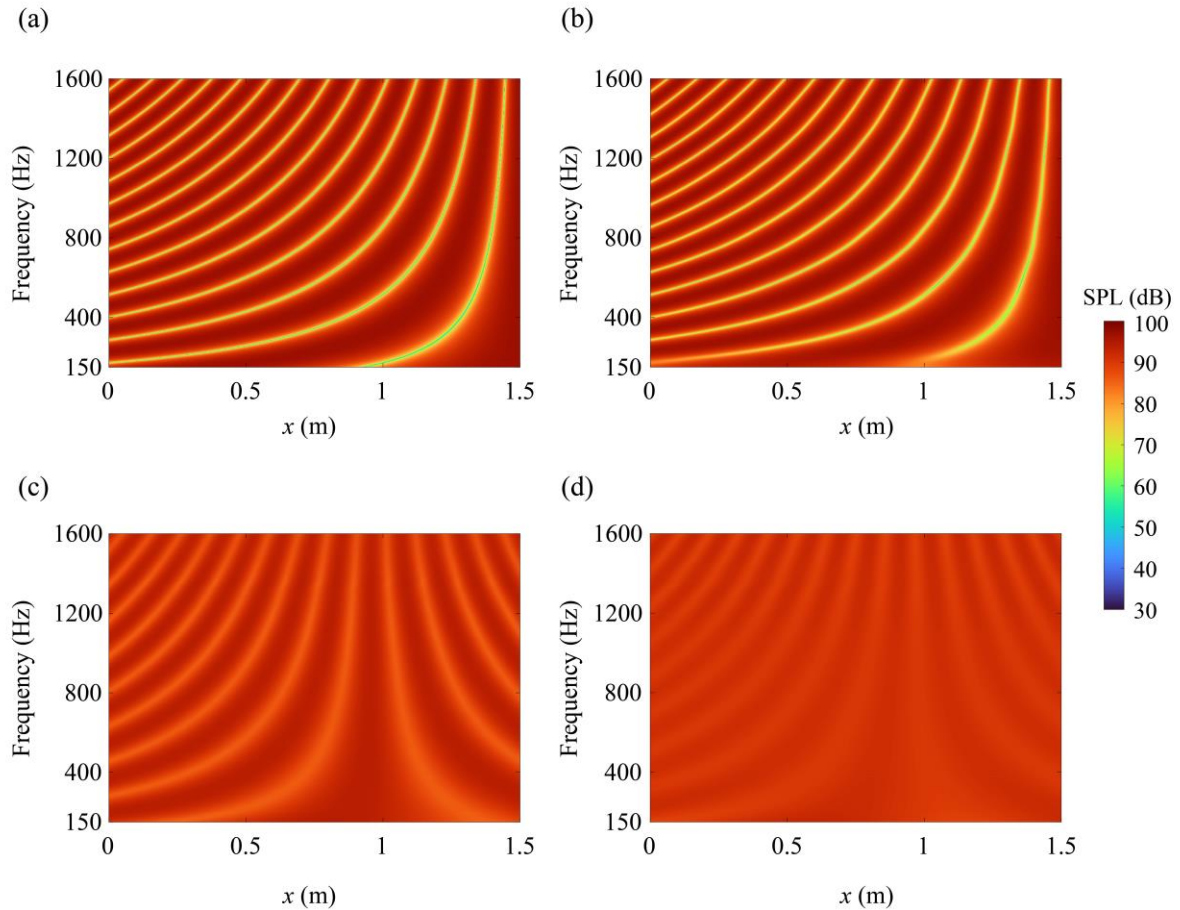
353



354

355 FIG. 6. (Color online) Setting various values of the target reflection coefficient R_0 in the error
 356 signal to achieve different sound absorption performance. (a) Acoustic absorption spectra for
 357 different R_0 values. (b) Comparison of the remaining amplitude of the reflected wave after
 358 active and passive absorption. (c) Comparison of measured average absorption coefficients
 359 with theoretical values.

360



361

362 FIG. 7. (Color online) The SPL distribution in the waveguide when the active absorber has
 363 different target reflection coefficients R_0 . (a) The hard boundary imposed at the right end of the
 364 waveguide for comparison. (b) Passive absorption with the active absorber turned off. (c)
 365 Active absorption with $R_0 = 0.5$. (d) Active absorption with $R_0 = 0$, corresponding to perfect
 366 absorption.

367

368 Subsequently, the effect of the active absorber on the sound field distribution in the tube is
 369 analyzed in detail. Utilizing the finite element model developed with commercial software
 370 COMSOL (see detailed model in Supplementary Note S1), and imposing the experimentally
 371 measured interfacial impedance of the active absorber at the right end of the waveguide, the
 372 sound pressure level (SPL) distribution in the tube for various target reflection coefficients R_0
 373 of the active absorber can be obtained, as shown in Fig. 7. Fig. 7(a) illustrates the SPL

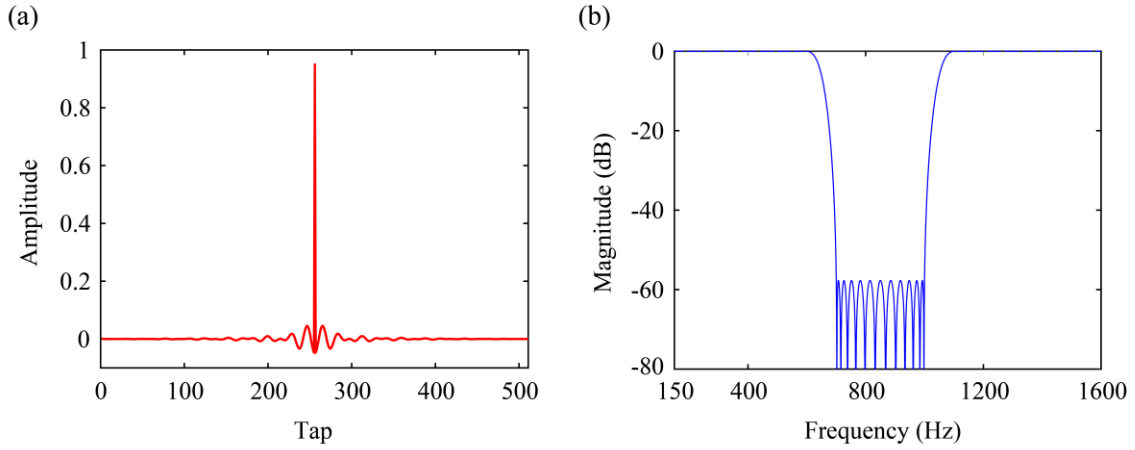
374 distribution in the tube with a hard boundary imposed at the waveguide's right end. Significant
375 standing wave features can be observed, indicating a highly inhomogeneous sound field. Fig.
376 7(b) shows the SPL distribution when the active absorber is off, relying only on the
377 loudspeaker's passive absorption capability. According to Fig. 5(a), since the loudspeaker only
378 has limited absorbing ability at 165 Hz and almost none at other frequencies, the sound field
379 distribution in the tube is still a standing wave field with large fluctuation. When the active
380 absorber is turned on and the target reflection coefficient $R_0 = 0.5$ is set, the SPL distribution
381 is illustrated in Fig. 7(c). The result demonstrates significantly reduced fluctuation within all
382 the 150–1600 Hz band. Setting the target reflection coefficient $R_0 = 0$ further homogenizes the
383 sound field, as shown in Fig. 7(d). These results indicate the great potential of the designed
384 active absorber for modulating sound field characteristics in confined spaces.

385

386 **B. Realization of spectrally tunable broadband sound absorption**

387 By employing a shaping filter $\mathbf{f}(n)$, the active absorber can achieve broadband sound
388 absorption with spectrally tunable characteristics. The time-domain impulse response and
389 amplitude-frequency response of a 512-tapped band-stop shaping filter $\mathbf{f}(n)$ are depicted in Fig.
390 8(a) and Fig. 8(b), respectively. $\mathbf{f}(n)$ has a stopband frequency range of 700–1000 Hz, and its
391 use to filter the error signal means that there is no need to eliminate the reflected wave within
392 700–1000 Hz. This characteristic is particularly useful in cases where higher reflection in a
393 particular band is desired.

394



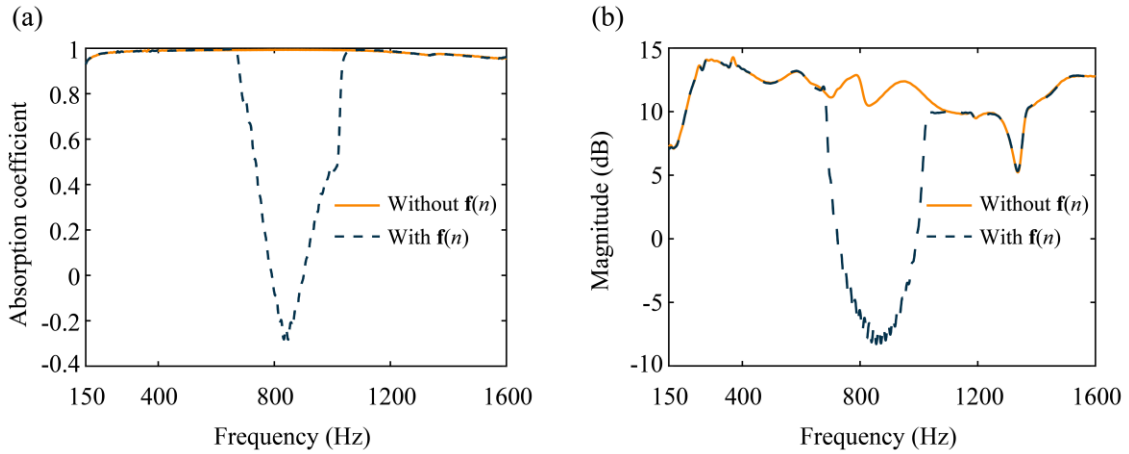
395

396 FIG. 8. (Color online) Designed band-stop shaping filter $\mathbf{f}(n)$. (a) Time-domain impulse
 397 response of $\mathbf{f}(n)$. (b) Amplitude-frequency response of $\mathbf{f}(n)$.

398

399 By setting the target reflection coefficient $R_0 = 0$ in Eq. (21) and filtering the error signal
 400 with the shaping filter $\mathbf{f}(n)$, the measured sound absorption spectrum is shown in Fig. 9(a).
 401 Comparing the active absorption effect before and after applying the shaping filter, a noticeable
 402 reduction of absorption performance within the stopband range of the filter can be observed.
 403 This reduction indicates the enhanced reflection of sound waves within this frequency range,
 404 consistent with the anticipated outcome. With the shaping filter $\mathbf{f}(n)$ utilized, the active absorber
 405 exhibits an average absorption coefficient of merely 0.15 within the 700–1000 Hz band, while
 406 other bands remain almost unaffected, achieving an average absorption coefficient of up to
 407 0.97. The spectrally tunable capacity stems from that the response of the control filter $\mathbf{w}(n)$
 408 within the stopband range is constrained, as illustrated in Fig. 9(b). Within the partial stopband
 409 range, the absorption coefficient may exhibit slight negativity, attributed to the controller's
 410 response not fully constrained to zero. This amplifies the reflection wave within the stopband
 411 compared to the fully passive case, in line with our design objective. The excessive reflection
 412 wave, on the other hand, can be alleviated by incorporating a fine-tuned shaping filter design
 413 or passive absorption materials if it is not desired.

414



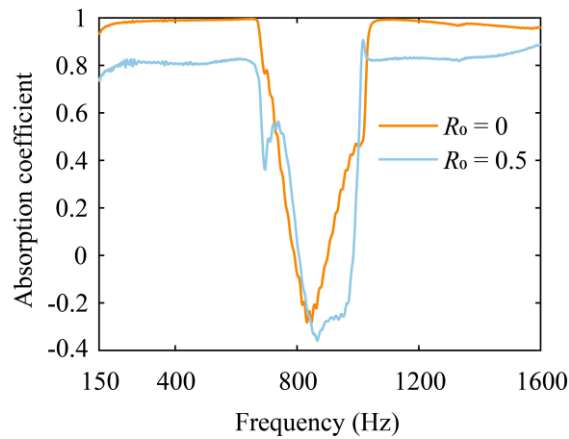
415

416 FIG. 9. (Color online) Comparison of sound absorption obtained with and without the shaping
 417 filter $f(n)$. (a) Spectra of absorption coefficient. (b) Amplitude-frequency response of the
 418 control filter.

419

420 Assigning different values to the target reflection coefficient R_0 in Eq. (21), the proposed
 421 active absorber achieves not only a tunable sound absorption spectrum but also modulation of
 422 the absorption coefficient in the passband. Fig. 10 compares the sound absorption effects for
 423 $R_0 = 0$ and $R_0 = 0.5$. When $R_0 = 0.5$, the absorption coefficient within the passband decreases
 424 accordingly, with an average absorption coefficient of 0.81, closely aligning with the
 425 theoretical value of $A_0 = 1 - |R_0|^2 = 0.75$. Therefore, the system demonstrates the ability to
 426 achieve broadband sound absorption performance with a flexibly tunable spectrum.
 427 Furthermore, a variety of absorption spectra can be synthesized by simply changing the shaping
 428 filter $f(n)$. Such an approach offers tremendous flexibility in reverse engineering by first
 429 defining the desired absorption spectrum and then adjusting the target reflection coefficient R_0
 430 and shaping filter $f(n)$ to match this spectrum.

431



432

433 FIG. 10. (Color online) Comparison of the sound absorption effect achieved by setting the
 434 target reflection coefficient R_0 to 0 and 0.5 in the error signal when utilizing the shaping filter
 435 $\mathbf{f}(n)$.

436

437 IV. CONCLUSIONS

438 This study presents an active absorber with flexible tunability in a one-dimensional
 439 standing wave tube. The two-microphone method is employed to separate the incident and
 440 reflected waves so that the error signal can be synthesized, enabling broadband adjustment of
 441 the acoustic absorption performance. This active absorber demonstrates remarkable near-
 442 perfect absorption within the 150–1600 Hz frequency band, with an average absorption
 443 coefficient of 0.98. Through manipulation of the target reflection coefficient in the error signal,
 444 the absorber achieves a tunable absorption coefficient spanning from 0 to 1 across more than
 445 three octave bands. Experimental results closely align with theoretical predictions. Utilizing
 446 the FeLMS algorithm with a band-stop filter, this active absorber obtains spectrally tunable
 447 broadband sound absorption, selectively reflecting specific frequency bands while absorbing
 448 the rest. By adjusting the target reflection coefficient in the error signal, the absorption
 449 coefficient in the passband is also customizable. Importantly, these modulation capabilities are
 450 realized solely through programming in the digital controller, without any alterations to the

451 physical structure of the active absorber. Although the active absorber has only been
452 demonstrated in a one-dimensional waveguide, the concept applies to higher dimensions in
453 which a large-area active absorber array can be expected by combining more units.⁴⁶ The
454 obtained findings highlight the flexible nature of the designed active absorber, promising
455 versatile solutions for controlling acoustic environments in confined spaces and offering
456 insights for potential applications in other scenarios.

457

458 **ACKNOWLEDGMENTS**

459 This work was supported by the National Natural Science Foundation of China (Grant No.
460 12274221).

461

462 **AUTHOR DECLARATIONS**

463 **Conflict of Interest**

464 The authors declare that they have no conflict of interest

465

466 **DATA AVAILABILITY**

467 The data that support the findings of this study are available from the corresponding author
468 upon reasonable request.

469

470 **REFERENCES**

471 ¹M. Cairoli, “Architectural customized design for variable acoustics in a Multipurpose
472 Auditorium,” *Appl. Acoust.* **140**, 167–177 (2018).

473 ²H. Kuttruff, *Room Acoustics*. (Crc Press, Boca Raton, 2016).

474 ³A. Merkel, G. Theocharis, O. Richoux, V. Romero-García, and V. Pagneux, “Control of
475 acoustic absorption in one-dimensional scattering by resonant scatterers,” *Appl. Phys. Lett.* **107**,

476 [244102 \(2015\)](#).

477 ⁴Z.X. Xu, H.Y. Meng, A. Chen, J. Yang, B. Liang, and J.C. Cheng, “Tunable low-frequency
478 and broadband acoustic metamaterial absorber,” *J. Appl. Phys.* **129**, 094502 (2021).

479 ⁵J.F. Li, W.Q. Wang, Y.B. Xie, B.I. Popa, and S.A. Cummer, “A sound absorbing metasurface
480 with coupled resonators,” *Appl. Phys. Lett.* **109**, 091908 (2016).

481 ⁶S. Huang, X. Fang, X. Wang, B. Assouar, Q. Cheng, and Y. Li, “Acoustic perfect absorbers
482 via Helmholtz resonators with embedded apertures,” *J. Acoust. Soc. Am.* **145**, 254–262 (2019).

483 ⁷H. Ding, N. Wang, S. Qiu, S. Huang, Z. Zhou, C. Zhou, B. Jia, and Y. Li, “Broadband acoustic
484 meta-liner with metal foam approaching causality-governed minimal thickness,” *Int. J. Mech.
485 Sci.* **232**, 107601 (2022).

486 ⁸H. Ryoo and W. Jeon, “Broadband sound absorption using multiple hybrid resonances of
487 acoustic metasurfaces,” *Int. J. Mech. Sci.* **229**, 107508 (2022).

488 ⁹Z. Zhou, S. Huang, D. Li, J. Zhu, and Y. Li, “Broadband impedance modulation via non-local
489 acoustic metamaterials,” *Natl. Sci. Rev.* **9**, nwab171 (2022).

490 ¹⁰Z. Mei, X. Li, Y. Lyu, J. Sang, X. Cheng, and J. Yang, “Broadband sound absorption based
491 on impedance decoupling and modulation mechanisms,” *J. Acoust. Soc. Am.* **154**, 3479–3486
492 (2023).

493 ¹¹C. Shao, Y.Z. Zhu, H.Y. Long, C. Liu, Y. Cheng, and X.J. Liu, “Metasurface absorber for
494 ultra-broadband sound via over-damped modes coupling,” *Appl. Phys. Lett.* **120**, 083504
495 (2022).

496 ¹²H.Y. Long, Y. Cheng, J.C. Tao, and X.J. Liu, “Perfect absorption of low-frequency sound
497 waves by critically coupled subwavelength resonant system,” *Appl. Phys. Lett.* **110**, 023502
498 (2017).

499 ¹³C.R. Chen, Z.B. Du, G.K. Hu, and J. Yang, “A low-frequency sound absorbing material with
500 subwavelength thickness,” *Appl. Phys. Lett.* **110**, 221903 (2017).

501 ¹⁴Y. Li and B.M. Assouar, “Acoustic metasurface-based perfect absorber with deep
502 subwavelength thickness,” *Appl. Phys. Lett.* **108**, 063502 (2016).

503 ¹⁵C. Zhang and X.H. Hu, “Three-Dimensional Single-Port Labyrinthine Acoustic Metamaterial:
504 Perfect Absorption with Large Bandwidth and Tunability,” *Phys. Rev. Appl.* **6**, 064025 (2016).

505 ¹⁶M. Yang, S.Y. Chen, C.X. Fuab, and P. Sheng, “Optimal sound-absorbing structures,” *Mater.*
506 *Horiz.* **4**, 673–680 (2017).

507 ¹⁷H.Y. Long, C. Shao, C. Liu, Y. Cheng, and X.J. Liu, “Broadband near-perfect absorption of
508 low-frequency sound by subwavelength metasurface,” *Appl. Phys. Lett.* **115**, 103503 (2019).

509 ¹⁸H. Long, C. Liu, C. Shao, Y. Cheng, K. Chen, X. Qiu, and X. Liu, “Subwavelength broadband
510 sound absorber based on a composite metasurface,” *Sci. Rep.* **10**, 13823 (2020).

511 ¹⁹C. Liu, Z. Yang, X. Liu, J.H. Wu, and F. Ma, “Ultra-broadband acoustic absorption with
512 inhomogeneous high-order Fabry–Pérot resonances,” *APL Mater.* **11**, 101122 (2023).

513 ²⁰K. Donda, Y.F. Zhu, S.W. Fan, L.Y. Cao, Y. Li, and B. Assouar, “Extreme low-frequency
514 ultrathin acoustic absorbing metasurface,” *Appl. Phys. Lett.* **115**, 173506 (2019).

515 ²¹J. Mei, G. Ma, M. Yang, Z. Yang, W. Wen, and P. Sheng, “Dark acoustic metamaterials as
516 super absorbers for low-frequency sound,” *Nat. Commun.* **3**, 756 (2012).

517 ²²G. Ma, M. Yang, S. Xiao, Z. Yang, and P. Sheng, “Acoustic metasurface with hybrid
518 resonances,” *Nat. Mater.* **13**, 873–878 (2014).

519 ²³M. Yang, C. Meng, C.X. Fu, Y. Li, Z.Y. Yang, and P. Sheng, “Subwavelength total acoustic
520 absorption with degenerate resonators,” *Appl. Phys. Lett.* **107**, 104104 (2015).

521 ²⁴Z. Lu, M. Shrestha, and G.-K. Lau, “Electrically tunable and broader-band sound absorption
522 by using micro-perforated dielectric elastomer actuator,” *Appl. Phys. Lett.* **110**, 182901 (2017).

523 ²⁵Y. Aurégan, “Ultra-thin low frequency perfect sound absorber with high ratio of active area,”
524 *Appl. Phys. Lett.* **113**, 201904 (2018).

525 ²⁶W. Ao, J. Ding, L. Fan, and S.-y. Zhang, “A robust actively-tunable perfect sound absorber,”

526 Appl. Phys. Lett. **115**, 193506 (2019).

527 ²⁷S.C. Qu, M. Yang, Y.F. Xu, S.W. Xiao, and N.X. Fang, “Reverberation time control by
528 acoustic metamaterials in a small room,” *Build. Environ.* **244**, 110753 (2023).

529 ²⁸Y.F. Zhu, S.W. Fan, L.Y. Cao, K. Donda, and B. Assouar, “Acoustic Meta-Equalizer,” *Phys.*
530 *Rev. Appl.* **14**, 014038 (2020).

531 ²⁹C. Olivier, A. Maddi, G. Poignand, and G. Penelet, “Asymmetric transmission and coherent
532 perfect absorption in a periodic array of thermoacoustic cells,” *J. Appl. Phys.* **131**, 244701
533 (2022).

534 ³⁰A. Maddi, C. Olivier, G. Poignand, G. Penelet, V. Pagneux, and Y. Aurégan, “Frozen sound:
535 An ultra-low frequency and ultra-broadband non-reciprocal acoustic absorber,” *Nat. Commun.*
536 **14**, 4028 (2023).

537 ³¹H.K. Zhang, Q.Y. Wang, M. Fink, and G.C. Ma, “Optimizing multi-user indoor sound
538 communications with acoustic reconfigurable metasurfaces,” *Nat. Commun.* **15**, 1270 (2024).

539 ³²T.T. Koutserimpas, E. Rivet, H. Lissek, and R. Fleury, “Active Acoustic Resonators with
540 Reconfigurable Resonance Frequency, Absorption, and Bandwidth,” *Phys. Rev. Appl.* **12**,
541 054064 (2019).

542 ³³C. Cong, J. Tao, and X. Qiu, “A Multi-Tone Sound Absorber Based on an Array of Shunted
543 Loudspeakers,” *Appl. Sci.* **8**, 2484 (2018).

544 ³⁴P. Zhang, C. Cong, J. Tao, and X. Qiu, “Dual frequency sound absorption with an array of
545 shunt loudspeakers,” *Sci. Rep.* **10**, 10806 (2020).

546 ³⁵Y. Zhang, Y.-J. Chan, and L. Huang, “Thin broadband noise absorption through acoustic
547 reactance control by electro-mechanical coupling without sensor,” *J. Acoust. Soc. Am.* **135**,
548 2738–2745 (2014).

549 ³⁶Y. Zhang, C. Wang, and L. Huang, “Tuning of the acoustic impedance of a shunted electro-
550 mechanical diaphragm for a broadband sound absorber,” *Mech. Syst. Sig. Process.* **126**, 536–

551 552 (2019).

552 ³⁷J. Tao, R. Jing, and X. Qiu, “Sound absorption of a finite micro-perforated panel backed by a
553 shunted loudspeaker,” *J. Acoust. Soc. Am.* **135**, 231–238 (2014).

554 ³⁸X. Li, Z. Cao, Z. Li, and B. Liu, “Sound absorption of a shunt loudspeaker on a perforated
555 plate,” *Appl. Acoust.* **193**, 108776 (2022).

556 ³⁹Z. Cao, X. Li, and B. Liu, “Broadband sound absorption of a hybrid absorber with shunt
557 loudspeaker and perforated plates,” *Appl. Acoust.* **203**, 109185 (2023).

558 ⁴⁰R. Boulandet and H. Lissek, “Toward broadband electroacoustic resonators through
559 optimized feedback control strategies,” *J. Sound Vibr.* **333**, 4810–4825 (2014).

560 ⁴¹E. Rivet, S. Karkar, and H. Lissek, “Broadband Low-Frequency Electroacoustic Absorbers
561 Through Hybrid Sensor-/Shunt-Based Impedance Control,” *IEEE Trans. Control Syst. Technol.*
562 **25**, 63–72 (2017).

563 ⁴²S. Sergeev, R. Fleury, and H. Lissek, “Ultrabroadband sound control with deep-
564 subwavelength plasmacoustic metalayers,” *Nat. Commun.* **14**, 2874 (2023).

565 ⁴³M. Volery, X.X. Guo, and H. Lissek, “Robust direct acoustic impedance control using two
566 microphones for mixed feedforward-feedback controller,” *Acta Acustica.* **7**, 2 (2023).

567 ⁴⁴S. Beyene and R.A. Burdisso, “A new hybrid passive–active noise absorption system,” *J.*
568 *Acoust. Soc. Am.* **101**, 1512–1515 (1997).

569 ⁴⁵P. Cobo, A. Fernández, and O. Doutres, “Low-frequency absorption using a two-layer system
570 with active control of input impedance,” *J. Acoust. Soc. Am.* **114**, 3211–3216 (2003).

571 ⁴⁶P. Cobo and M. Cuesta, “Measuring hybrid passive-active sound absorption of a
572 microperforated liner at oblique incidence,” *J. Acoust. Soc. Am.* **125**, 185–190 (2009).

573 ⁴⁷F. An, P. Zhao, X. Li, Q. Wu, and B. Liu, “Active impedance control of a loudspeaker and its
574 parallel combination with porous materials for broadband sound absorption,” *Mech. Syst. Sig.*
575 *Process.* **206**, 110909 (2024).

576 ⁴⁸S.M. Kuo and J.M. Tsai, “Residual noise shaping technique for active noise-control systems,”
577 J. Acoust. Soc. Am. **95**, 1665–1668 (1994).
578 ⁴⁹X. Ma, D. Yurchenko, K. Chen, L. Wang, Y. Liu, and K. Yang, “Structural acoustic controlled
579 active micro-perforated panel absorber for improving wide-band low frequency sound
580 absorption,” Mech. Syst. Sig. Process. **178**, 109295 (2022).
581 ⁵⁰S. Elliott, *Signal Processing for Active Control*. (Academic Press, London, 2001).
582 ⁵¹A.V. Oppenheim and R.W. Schaffer, *Discrete-time signal processing*. (Prentice Hall Press,
583 USA, 1999).